MDPI

Article

Experimental investigation of the unsteady stator/rotor wake characteristics downstream of an axial air turbine

Daniel Duda [1]*, Tomáš Jelínek[3], Petr Milčák[4], Martin Němec[3], Václav Uruba [1,2], Vitalii Yanovych [1,2] and Pavel Žitek[1]

[1] University of West Bohemia in Pilsen; dudad@kke.zcu.cz
[2] Czech Academy of Sciences; uruba@it.cas.cz
[3] Czech Aerospace Research Centre; jelinek@vzlu.cz
[4] Doosan Škoda Power; petr.milcak@doosan.com
* Correspondence: dudad@kke.zcu.cz; Tel.: +420 377 638 146

Version June 21, 2021 submitted to Journal Not Specified

Abstract: The feasibility study of the velocity field measurements using Particle Image Velocimetry (PIV) method in an axial air turbine model is presented. The wakes past the blades of the rotor wheel were observed using the PIV technique. Data acquisition was synchronized with the shaft rotation, thus the wakes are phase averaged for statistical studies. The interaction of the rotor blade wakes with the stator ones were investigated by changing the stator wheel angle. The measurement planes are located just behind the rotor blades covering approximately 3×3 cm in axial $\times$ tangential directions. The spatial correlation function suggests that the resolution used is sufficient for the large-scale flow-patterns only, but not for the small ones. The scales of fluctuations correspond to the shear layer thickness at the mid-span plane, but close to the end-wall, they contain larger structures caused by the secondary flows. The length-scales of the fluctuations under off-design conditions display the dependence on the area of the stator and rotor wakes cross-sections, which depend on their angle. The obtained experimental data is to be used for validation of mathematical simulation results in the future.

Keywords: Particle Image Velocimetry ; Turbine ; Turbine test facility ; Length-scale ; PIV ; Turbomachinery ; Wake

1. Introduction

Due to the crucial importance of steam turbines in the current "electric age", there are a large number of scientific studies concerning the flow through these admirable machines. The flow inside an axial turbine is highly dynamical, consisting of an important periodical component connected with moving wakes behind the rotor blades and a truly turbulent component. These two components play very different roles in the flow dynamics including mixing properties and flow stability behavior. The effect of periodicity on the stability of a laminar boundary layer was studied intensively in the past mainly in simplified situations using both experimental and mathematical models, see e.g. [1].

The majority of the studies in axial turbomachines is performed using pressure measurements, which is the most robust and straight forward method [2]. Typically, simple or complex (multi-hole) pressure probes are used, in combination with the moving point measurements strategy. Subsequently, the pressure and/or velocity fields are reconstructed from the multiple point measurements. This method is suitable only for the evaluation of statistical characteristics supposing stationarity during the whole measuring procedure and application of averaging or phase averaging strategies. An example of this type of measurement could be find in the pioneering work reported in [3] or elsewhere. The

development of *fast response aerodynamic probe* FRAP [4] allows to resolve high frequency pressure fluctuations up to tens of kilohertz [5] similarly as hot-wire anemometry, which is another of the promising possibilities characterized by high frequency response up to hundreds of kilohertz, see e.g. in [6].

Optical methods are used very seldom in axial machines, because of the problematic access. The first attempts of optical methods applications in axial turbomachines were made only to visualize the flow – see [7]. The optical density detecting methods as shadowgraph, schlieren and interferometry, are frequently used in turbomachinery, however only in planar configurations in linear stationary cascades – see e.g. [8]. These methods are not suitable for fully 3D cases, as they perform averaging in the trans-illumination direction. Relatively easy application offers another optical method, the Laser Doppler Anemometry (hereinafter LDA). This method requires optical access through a single window only – see e.g. [9]. However, the LDA method is of the point measurement type and needs a traversing strategy and averaging to explore a multidimensional area, the same as the pressure measurement method mentioned above. In contrast to that, Particle Image Velocimetry (PIV) is a typical 2D method exploring the plane of measurement, however it requires much more complex optical access consisting of two perpendicular windows at least, one for the laser and the other for the camera. There are only a few attempts to solve this tough technical problem. For example, in [10], the stereo PIV system was applied in combination with an endoscope for the laser light sheet for the study of the blade row interaction. Lang et al. [11] used stereoscopic PIV to explore the flow between the rotor and stator wheel. They directly observed vortices in instantaneous velocity fields and their interaction with shock waves (their experiment was transonic, while the present experiment is carried out at an isentropic stage Mach number around 0.4). Jones et al. [12] constructed a very advanced test turbine facility equipped with the CO_2 PLIF system with optical access through a borescope. Yun et al. [13,14] used Stereo PIV to study the flow in a rotor shroud cavity.

A comprehensive application of the above measurement techniques is shown in the studies of Göttlich and Woisetschläger. The authors focused on the experimental and numerical investigations of the evolution of turbulent flow in transonic turbines. In particular, in [15–17] the patterns of vortex emissions at the trailing edge of the stator and rotor blades, as well as the interaction of their blade rows were assessed in detail using LDA and PIV. In [18,19] the authors used these methods to clearly record the distributed velocity, flow angle, and turbulence characteristics depending on the position of the stator and rotor blades. In some cases, the authors also used a Laser Vibrometer (LV) to measure the frequency of density fluctuations in the stator wake downstream of a rotor [20,21]. But, this technique is mainly used in combination with other measurement methods as, for example, with stereoscopic PIV, which allows to identify the turbulence of the flow field during the passage of the rotor blade.

The axial air turbine model used in the present investigation is described in detail in [22,23]. It was equipped with a system of windows and mirrors in the flow section. Using the single camera PIV method, a set of instantaneous 2D velocity fields was taken covering a finite field of view (FoV) located behind the rotor wheel [24,25]. Due to the instantaneity of velocity fields, this method offers the possibility of in-depth spatial statistics of the flow pattern.

2. Experimental setup

2.1. Test facility

The experimental turbine facility at the Czech Aerospace Research Centre in Prague (VZLÚ) is a single stage turbine with air as a working fluid. The test rig is a part of a closed-loop aerodynamic wind tunnel. It allows to independently change pressure ratio, Reynolds number and rotational speed of the turbine. The pressure ratio is controlled by the rotational speed of a twelve-stage radial compressor driven by a 1.3 MW electric motor of the company ČKD. The Reynolds number can be changed by the pressure level, which is maintained by a system of vacuum pumps. Air temperature and humidity

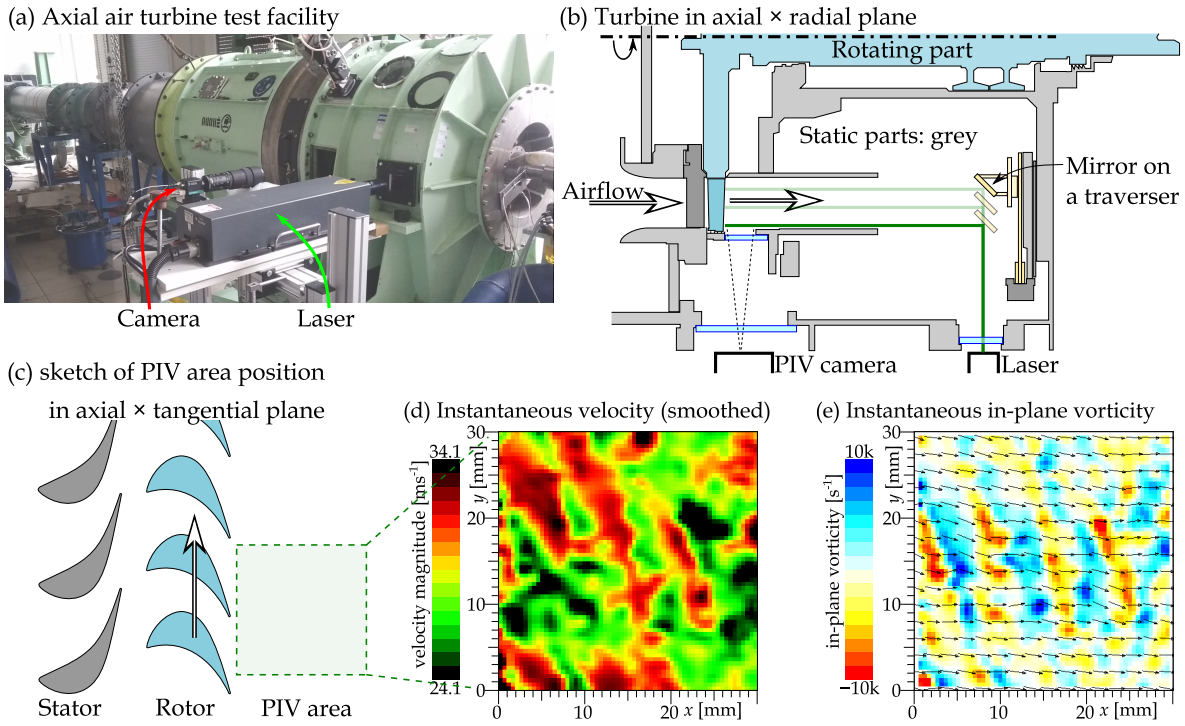

Figure 1. Photograph (a) of the test facility. The air flows from left to right. Panel (b) sketches the turbine in the axial × radial plane, the path of the laser sheet is manipulated by using a motorized traverser. Panel (c) is a sketch of the position of the area studied by PIV relative to the stator and rotor blades. Panel (d) represents an example of measured instantaneous velocity magnitude; for esthetic purposes, the displayed data are smoothed by Gauss function of halfwidth $\sigma = 0.5\,\mathrm{mm}$; the legend ranges by 5 m/s around the spatio-temporal average. Panel (e) shows an example of the instantaneous in-plane vorticity $\omega = \Delta u/\Delta y - \Delta v/\Delta x$ under nominal conditions at $u/c = 0.55$.

are controlled by inter-stage heat exchangers and a condenser dryer, respectively. The turbine stage rotational speed is controlled by a hydraulic dynamometer.

2.2. Turbine stage configuration

The turbine stage geometry represents a typical 30%-reaction stage with a nominal velocity ratio of $u/c = 0.55$ (where u is the circumferential mid-span rotor velocity and c the isentropic stage velocity) and a nominal stage isentropic Mach number $\mathrm{Ma} = 0.4$. The stage geometrical characterization is presented in table 1 [22]. The nominal rotation rate (denoted as $u/c = 0.55$ across this paper) is achieved at a rotational speed of $2800\,\mathrm{min}^{-1}$. The experiments at underload regime described in section 4.5 are performed at ratio $u/c = 0.7$ at rotational speed $3600\,\mathrm{min}^{-1}$. At overload regime of $u/c = 0.4$ at rotational speed $2000\,\mathrm{min}^{-1}$.

2.3. Particle Image Velocimetry

The experimental technique of *Particle Image Velocimetry* (PIV) is already a standard tool for aerodynamic research [2,26,27]. It is based on the optical observation of small *particles* following the flow and illuminated by a laser sheet. When the particles are small enough, their inertial time-scale is shorter than the flow time-scale (the ratio of which is the *Stokes number*) and therefore the particle is a good *tracer* suitable for all particle-based measurements.

A double solid state laser New Wave Solo generates pulses of duration 5 ns at a wavelength $\lambda = 532\,\mathrm{nm}$ (which corresponds to green color). The laser beam is defocused in one direction and slightly focused in the perpendicular direction by using a compact Lens system from the company

	Unit	Stator			Rotor IRv2		
N	[1]	66			82		
L	[mm]	78.5			80		
D_h	[mm]	440			440		
		hub	mid	tip	hub	mid	tip
t	[mm]	20.9	24.7	28.4	16.9	19.9	23.0
c_h	[mm]	32.9	38.8	44.6	23.0	24.5	26.0
B_{ax}	[mm]	24.3	29.2	32.6	22.6	22.1	21.2
β_{in}	[°]	90.0	90.0	90.0	26.0	42.0	65.0
β_{out}	[°]	15.5	17.0	15.5	21.7	20.2	18.1

Table 1. Parameters of the stator and rotor wheel. N is the number of blades, L denotes the blade height and D_h the hub diameter. Other parameters smoothly change along the blade height and thus they are explicitly written at the hub, at mid-span and at the blade tip. t means distance between neighboring blades, c_h represents the chord length and B_{ax} is its projection into axial direction, the input and output angles β_{in} and β_{out} are counted with respect to the tangential direction.

Plane	Diameter [mm]	High	FoV [mm]
R_{445}	445	$\frac{1}{16}$	32.6
R_{460}	460	$\frac{1}{4}$	32.1
R_{480}	480	$\frac{1}{2}$	31.0
R_{520}	520	1	29.2

Table 2. List of measurement planes denoted $R_{445} - R_{520}$, their radial location from the axis of the turbine (note that the endwall radius is 440 mm while the radius of the blade tips is 520 mm) and the corresponding size of field of view (FoV) of the camera focused into such plane.

Dantec. This laser sheet enters the turbine body through a window. Inside it is reflected from a metal-covered mirror mounted on a small traversing system allowing a simple change of the measuring area by shifting the mirror radially.

The FlowSense Mk II CCD camera distinguishes frames separated by a delay of 4 microseconds depending on the measuring conditions. The trigger signal is produced by the optical gate at the rotor shaft, therefore the frame-pairs are synchronized with the rotor angle allowing to perform the *phase averaging*. The maximum repeating frequency of frame pairs is 7.4 Hz, which is the hardware limit of the camera. The camera resolution of 2048×2048 pixels corresponds to the size of a square field of view in the range of $29 - 32$ mm, for more details see table 2.

The coordinate system is as follows: the axial coordinate is denoted x, the tangential y, while the radial coordinate is used only to designate the radii of measurement planes. The corresponding velocities are u for the axial component, v for the tangential one. The radial component is not measured. In all figures in this paper, the dominant axial velocity points from left to right; the trailing edges of rotor blades are just behind the left edge of the figures.

3. Issues related to the data quality

3.1. Troubles with covering glass

The most serious problem during the measurement was that of large droplets of seeding oil dirtying the covering glass between the inner and outer region of the diffuser. The hypothetical source of these large droplets is that the fine fog of oil droplets of the size of around $\sim (1 - 10) \cdot 10^{-6}$ m condensates on the surface of the fast moving rotor blades creating a continuous film. The liquid then moves due to the centrifugal force to the blade tips, where it detaches in the form of large droplets, which splash onto the glass. The glass first contains large areas, where measurements are impossible.

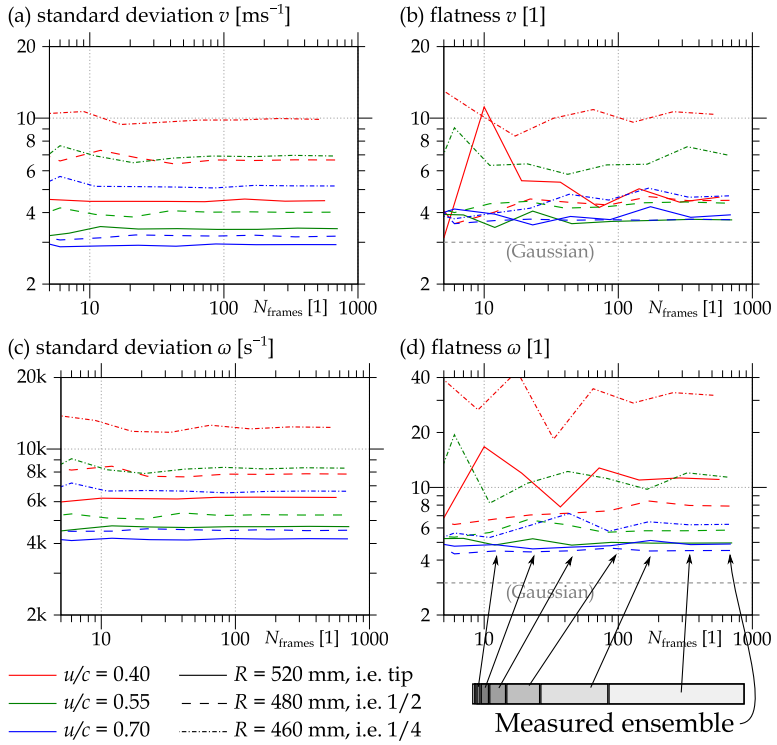

Figure 2. Dependence of the second and fourth statistical moment of tangential velocity and vorticity on the length N of different subsets of the measured ensemble.

With time it losses its transparency completely. Therefore this glass was removed leaving a large square hole in the body of the diffuser (it is the upper glass denoted as light-blue rectangle in the Figure 1(b)). This arrangement significantly changes the geometry, therefore a deeper discussion on the trustworthiness of the result was needed. A comparison of the measured velocity fields at tip radius with the same flow and acquisition parameters, but with and without the covering glass is shown and discussed in our conference contribution [28], which is available as *open access*. In that contribution, we observed that the flow characteristics remain unaffected by this rude change; the magnitude of the average velocity is the most affected property.

3.2. Check of the statistical quality

The number of obtained data is a very important issue to ensure statistically relevant results. Generally speaking, more is better, but technically, it does not need to be easy. During this study, about 700 snapshots were taken in each case. This amount is not ideally large, but it might be sufficient for convergence of statistical analysis.

To check this issue, It was decided to decrease the number of frames and to calculate the standard deviation (Figure 2(a,c)) and flatness (Figure 2(b,d)) of the tangential velocity v and of the in-plane vorticity ω for smaller ensembles. The smaller ensembles are generated by halving the rest of the previous halving. Therefore, a single snapshot appears only in one of those smaller ensembles (and, off-course, inside the original one), this scheme is sketched at the bottom of Figure 2.

The standard deviation converges pretty well, but higher moments naturally need better statistical quality, therefore they are suitable for testing it. Flatness is the fourth statistical moment calculated according to equation (4). In Figure 2(b), the flatness of the tangential velocity component is plotted; its value converges to the Gaussian limit of 3. The distribution of the radial vorticity is polynomial rather than Gaussian (compare to Figure 9). Thus the vorticity flatness might converge to a different limit, whose value is still a subject of research [29,30].

4. Results

4.1. Effect of stator wheel

The flow past a single turbine stage is affected not only by the wake of the rotor, but also by the wake of the upstream stator. The interaction of these two wake systems can be studied statistically by using the *phase averaging* of the data obtained at the same rotor angle. A slight rotation of the stator allowed to distinguish natural waves in the rotor wakes from those caused by the stator wakes as illustrated in Figure 3 presenting the phase averaged data at three different stator wheel positions.

In analogy to the grid turbulence, we can distinguish in each wake system the following regions: the *wakes* past the blade, the free *jets* past the cascade channel and the *shear layers* in between. The velocity magnitude is lower in the wakes, it is higher in the jets. The shear regions are characterized by an increase in the turbulent kinetic energy TKE; the shear layers quite soon overlay the entire wake region, while the live-time of the jets is longer. Even when both are turbulized, there is clear difference in the velocity between former wakes and jets[1].

In Figure 3 we can easily see systems of wake and jet structures past rotor and stator wheel overlaying each other. They are visible as alternating strips of higher and lower velocity. The rotor is responsible for the strips in top left $\rightarrow$ right bottom direction, while the stator produces the wider and weaker horizontal strips.

Note that this is not just a passive addition, as can be seen from the change of rotor strips angle in the jets or wakes of the stator. Much more important are these effects for the evolution of vortices in both wake systems. Note, that the stator wake is horizontal only at the nominal rotational speed.

The turbulent kinetic energy (TKE) shown in multiple figures in this paper is calculated by using the measured velocity components u and v, the third (radial) component is ignored. The TKE is calculated at each spatial point by using the ensemble of local velocity components:

$$\mathrm{TKE} = \frac{1}{2}\left(\left\langle u^2 \right\rangle - \langle u \rangle^2\right) + \frac{1}{2}\left(\left\langle v^2 \right\rangle - \langle v \rangle^2\right), \tag{1}$$

where $\langle . \rangle$ stands for ensemble averaging. Since TKE does not take into account the fluctuations in radial direction, its value is underestimated by approximately $1/3$. Additionally, fluctuations smaller than the interrogation area of the PIV method cannot be included in the TKE. On the other hand, the values of TKE are increased by the noise of the measurement, thus the estimation of something like a *true value* is not straight forward and therefore we prefer to keep the calculation procedure as simple as possible without including any artificial repair coefficients.

Under the nominal conditions ($u/c = 0.55$), the system of alternating jets and wakes past the stator can be highlighted by averaging along the axial direction, which averages out the stronger wake system past the rotor. The tangential profiles of *axially averaged* velocity magnitude $|v| = \sqrt{u^2 + v^2}$ and turbulent kinetic energy TKE are shown in Figure 4(b,c). In this profile, we can select various coordinates of interest, e.g. at the minimum or maximum of the velocity magnitude or at the maximum

[1] The sketch of the idea of combining systems of wakes and jets past rotor and stator wheel as if it was a grid turbulence

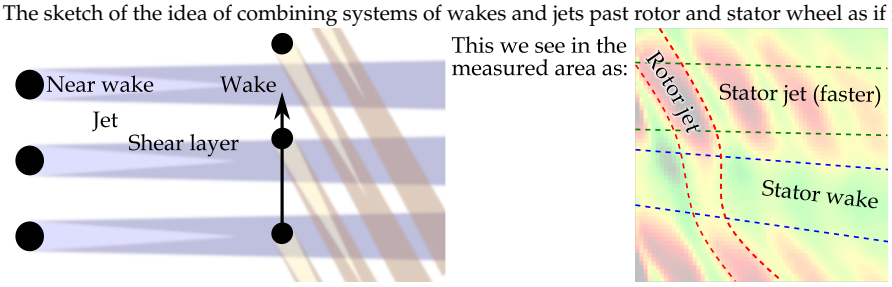

The approximate path of jet past past single rotor blade is depicted by red dashed lines; it is deformed as it crosses the faster and slower fluid in the stator jet and stator wake.

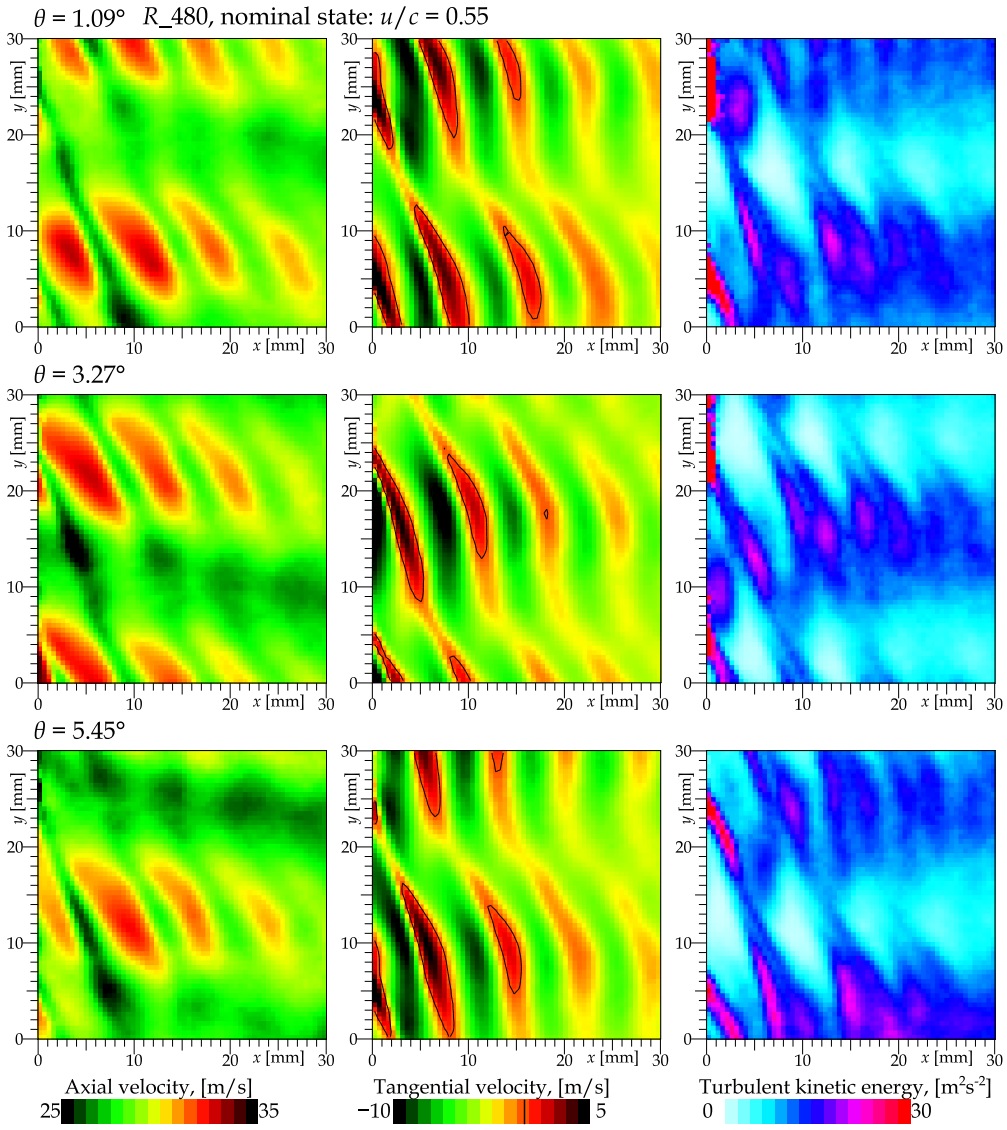

Figure 3. Average velocity fields obtained at different angle of the entire stator wheel to the measured area. First row displays the data at stator angle $\vartheta = 1.09°$ to some arbitrary reference position, second row shows data at $\vartheta = 3.27°$ and the third one at $\vartheta = 5.45°$. For the sake of clarity, there are not displayed the velocity vectors, just some of the statistical quantities displayed in color: first column shows the ensemble average of axial velocity component, second one the tangential velocity component (zero, i.e. pure axial motion, is highlighted by black isotach) and the third one the turbulent kinetic energy. These data are measured at nominal conditions in plane R_{480} at Mach number Ma $= 0.4$ and $u/c = 0.55$.

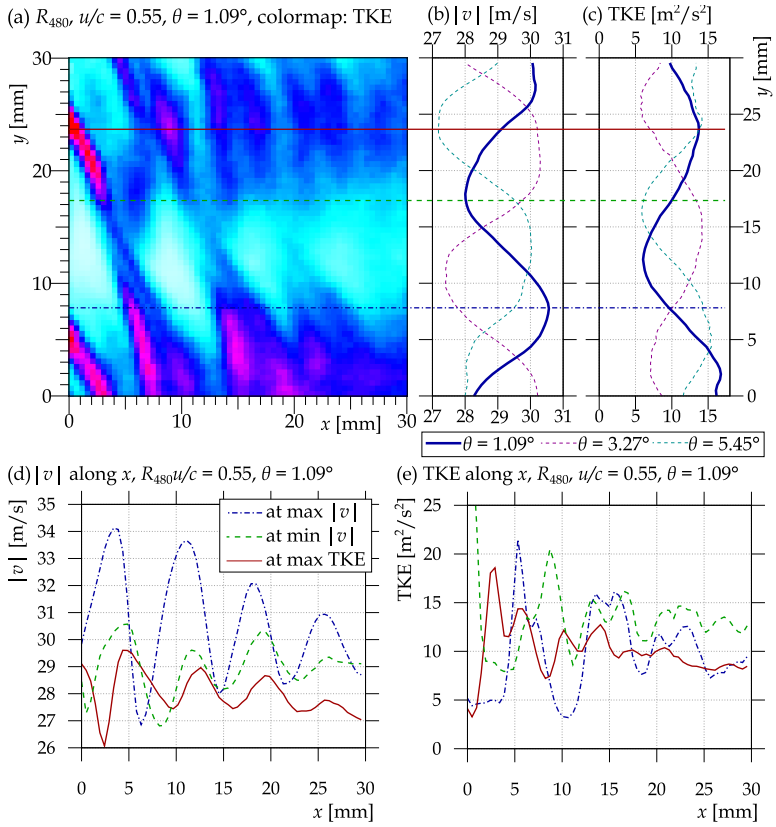

Figure 4. Stator wheel angle effect. Panel (a) shows the spatial distribution of the turbulent kinetic energy (TKE) (the exactly same data are shown in Figure 3), panel (b) shows the averages along axial direction of velocity magnitude w and panel (c) presents TKE. For comparison, there are displayed the profiles for different stator wheel angles as dashed lines. Three horizontal lines of interest are depicted by the blue dash-dotted, green dashed and red solid lines. The bottom panels (d, e) show the axial cuts of w and TKE at these three lines, namely at maximum average w , at minimal $|v|$ and at the maximum of TKE. This data set is measured at nominal state in plane R_{480} at Mach number Ma $= 0.4$, $u/c = 0.55$ and stator angle $\vartheta = 1.09°$.

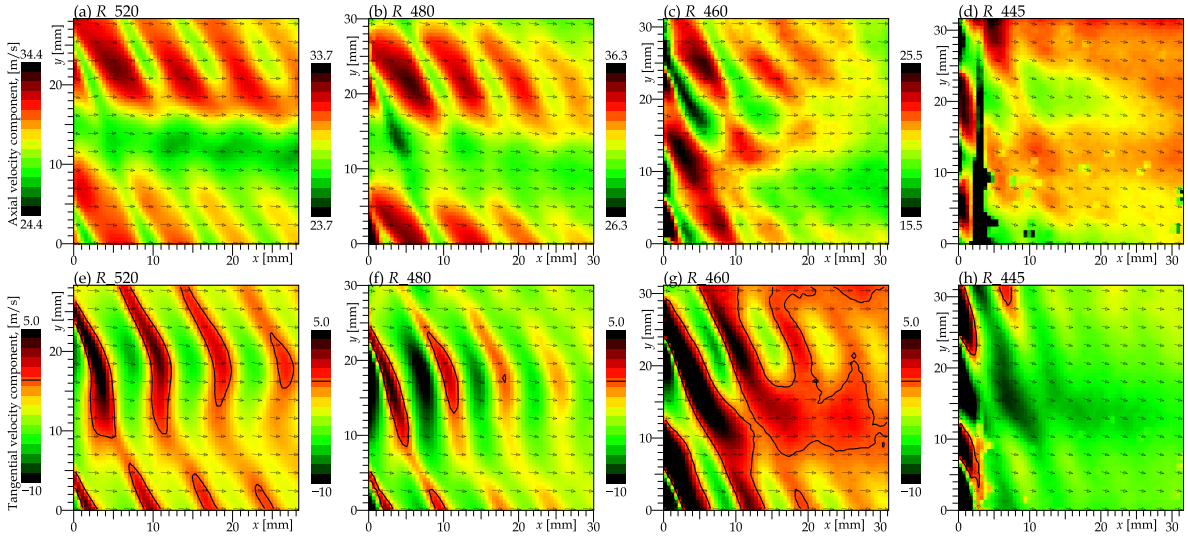

Figure 5. Ensemble averaged velocity at different radial planes. The colormap ranges by 5 m/s around the average axial velocity (top row), which is 29.4 m/s at the plane R_{520}, 28.7 at R_{480}, 31.3 at R_{460} and only 20.5 m/s at the plane R_{445}. The bottom row shows the tangential velocity component with depicted zero isotach (i.e. pure axial motion). Only every fifth vector is plotted. All states are nominal, i.e. $u/c = 0.55$ at Ma $= 0.4$, stator angle is $\vartheta = 3.27°$.

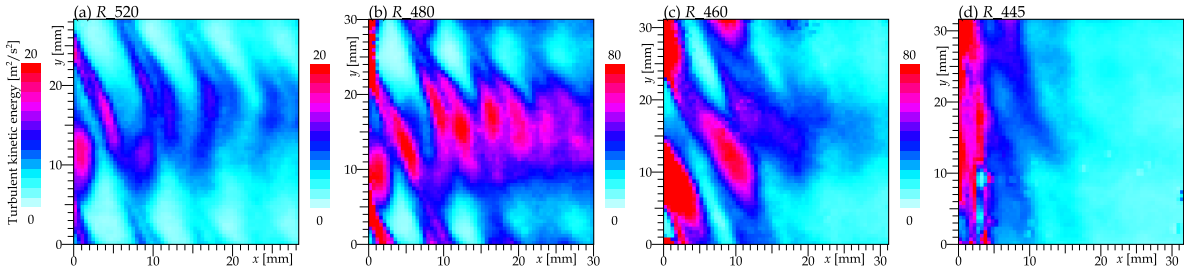

Figure 6. Maps of turbulent kinetic energy at different radial planes. Note that (a), (b) have different color maps ($0 - 20\,\mathrm{m^2 s^{-2}}$) than (c), (d) ($0 - 80\,\mathrm{m^2 s^{-2}}$). All states are nominal, i.e. $u/c = 0.55$ at Ma $= 0.4$, stator angle is $\vartheta = 3.27°$.

of TKE. They can be interpreted as the stator wake, stator jet and stator shear layer. The profiles of $|v|$ and TKE along the axial direction at the mentioned tangential coordinates are plotted in Figure 4(d,e). These profiles follow the stator wake system showing the wake system past rotor: note the large difference of the velocity magnitude along the stator jet (dash-dotted blue line in Figure 4(d,e)). Another interesting point to mention is the double peak of TKE (Figure 4(e)) caused by the pair of shear layers past the rotor, which are not yet connected.

4.2. Radial development

Exploring planes at different radii at nominal state, see Figures 5, 6, shows a quite homogeneous behavior with reasonably low turbulence at the tip plane R_{520}. At R_{480}, the stator wake structures become less dominant with increasing downstream distance when comparing it with the tip plane (R_{520}). This can be connected with the stronger turbulence there. Closer to the hub, the secondary flow effects start to be dominant, which decreases the observability of both the stator and rotor wake structures (Figure 5) and increases the turbulence level (Figure 6). Additionally, the quality of data at lowest radius (R_{445}) is decreased due to the optical distortions caused by focused non-flow structures

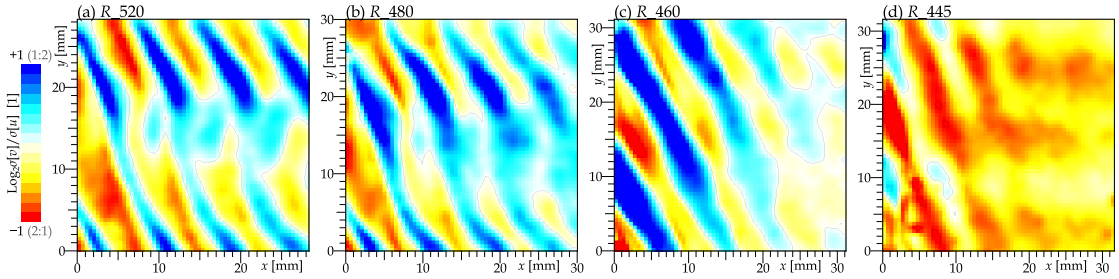

Figure 7. Maps of the ratio of fluctuations in tangential to fluctuations in axial direction. Bluer colors signify the dominance of tangential fluctuations over axial ones, redder colors represent areas with dominating axial fluctuations and the white means, that the fluctuations are isotropic. All states are nominal, i.e. $u/c = 0.55$ at Ma $= 0.4$, stator angle is $\vartheta = 3.27°$.

(surface roughness and oil droplets) at the inner body (at higher radii, such structures are defocused due to the large distance from the focus plane).

The anisotropy of fluctuations offers another very interesting aspect of turbulent flows. The full level of anisotropy can be investigated only in the case we know all three velocity components [31,32], which is not our case, as we measure only the axial and tangential velocity component. Even in such case, it is possible to evaluate the *degree of anisotropy* (DA) [33] based on two measured velocity components, judging which ones contain more fluctuations. Porreca et al. [9] present this parameter in the tangential $\times$ radial plane inside a multistage axial turbine. Gallego et al. [33] measure it in a wake past a single airfoil. The definition differs in the literature. Therefore we use the simple and symmetric definition of the ratio of the standard deviations of the two measured velocity components as it is used e.g. in Romano's work [34]

$$\mathrm{DA} = \log_2 \sqrt{\frac{\langle v^2 \rangle - \langle v \rangle^2}{\langle u^2 \rangle - \langle u \rangle^2}}. \tag{2}$$

In addition to Romano [34], the logarithm function is applied, which maps the interval $(0;\infty)$ with center in 1 to a symmetric interval $(-\infty;\infty)$ with center in 0. Thus in the Figure 7, the value of -1 reads a twice larger standard deviation of the axial velocity than that of the tangential velocity and vice versa.

The physical interpretation in a case of the wake past a single obstacle is, that the dominance of traverse velocity fluctuations is typical for *bluff body* wakes, where there forms a structure of alternating large-scale von Kármán vortices [35]. This is also the case of a single airfoil, or turbine blade [33]. But this is not the case here! First of all, let us note that the DA is almost isotropic in the stator wake behind the rotor, which can be explained by the effect of isotropization during the turbulence decay [36]. Secondly, the maxima of DA are located in the area occupied by fast interblade jets. But, the maxima of DA are shifted in axial direction with respect tot the maxima of the velocity magnitude displaying the positions of jets past the rotor wheel, see Figure 8 where a direct comparison for the mid-span plane is plotted. We are not able to explain it at this moment.

Among the different planes, the spatial distribution of DA more or less follows the stripped structure observable in other quantities at higher radii (R_{520} and R_{480}). At the plane R_{460}, the effect of stator wake weakens and the effect of rotor wakes dissipates faster within this quite small FoV. Close to the hub plane (R_{445}) we see the dominance of axial fluctuations, which are caused by the strength of secondary flow structures, which are naturally more developed in that direction.

4.3. Statistics

The statistical distributions of instantaneous tangential velocity component and instantaneous vorticity are plotted in Figure 9 for different radial planes. The data are taken from the entire field

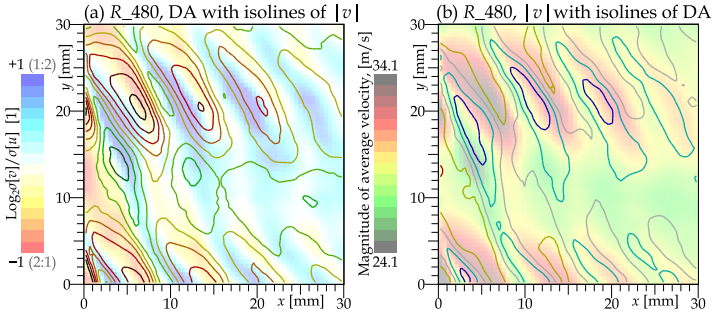

Figure 8. Direct comparison of spatial distribution of Degree of anisotropy DA with average velocity magnitude $|v|$. Plane R_{480}, Mach number Ma $= 0.4$, ratio $u/c = 0.55$ and stator angle $\vartheta = 3.27°$.

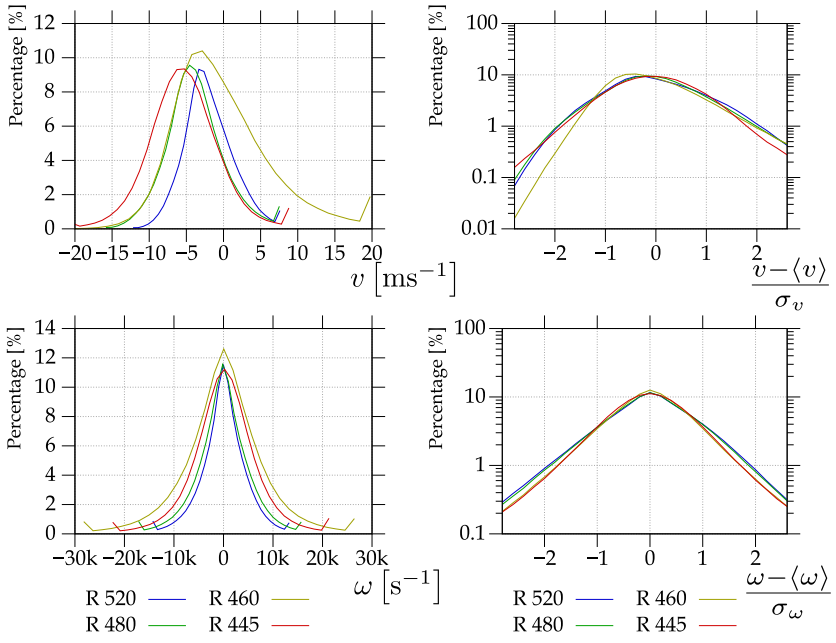

Figure 9. Histograms of tangential velocities (top row) and vorticities (bottom row) of the entire field of view at nominal state, i.e. $u/c = 0.55$ at Ma $= 0.4$, stator angle is $\vartheta = 3.27°$, planes are different. Right column shows the same data normalized by subtracting the average and dividing by the standard deviation in order to highlight the shape of distribution.

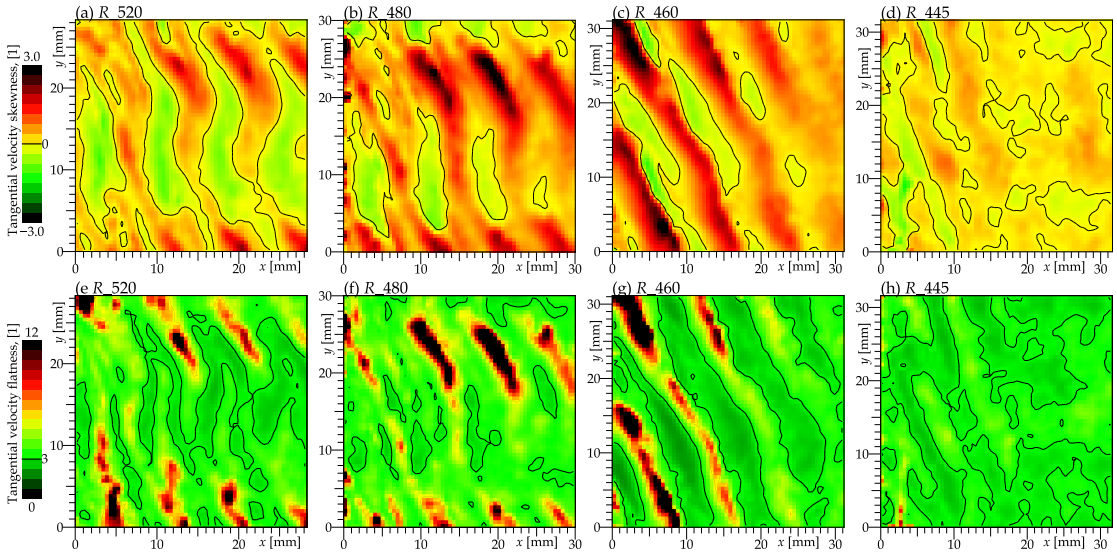

Figure 10. Maps of the skewness (third statistical moment) and flatness (fourth statistical moment) of tangential velocity component. The skewness of symmetrical distribution is equal to 0, the flatness of the Gauss function is equal to 3; those values are depicted by solid black lines.

of view. The case, which differs most from the rest, is surprisingly the plane R_{460}. Its asymmetry coefficient (skewness) of tangential velocity is calculated as

$$S\left[v\right] = \left\langle \frac{\left(v - \langle v \rangle\right)^3}{\sigma^3\left[v\right]} \right\rangle, \tag{3}$$

($\sigma\left[v\right]$ is the standard deviation of v) and it reaches the value of 1.36 at the plane R_{460}, while at the other planes it is 0.48, 0.57 and 0.69 at the plane R_{445}. This can be caused by the small oscillations of the wake patterns, which bring more deflected velocities from the jet areas into the areas of wakes, see Figure 10. This effect plays a role at every plane, but, at higher planes, the effect of increased skewness in the wakes is almost compensated by the opposite effect at the jets, while in the plane R_{460}, areas of negative skewness are smaller due to the deflection of the entire velocity field from the axial direction and thus smaller jet areas. Here can arise some recommendation for turbine designers: the wakes are too thick at this plane and the outgoing velocity could be larger in the counter-rotor direction (in order to push more momentum to the rotor). Why is the large skewness with combination of positive average tangential velocity wrong for the turbine? Positive skewness signifies that there are few events of value larger than average, which balance higher amount of events of value smaller than average. But the larger positive velocities ("positive" means co-rotating with the rotor wheel) produce square times more force *against* the rotor rotation.

In the hub plane R_{445}, the flow is dominated by secondary structures, which themselves are not far from a Gaussian distribution and are distributed almost symmetrically (skewness close to zero). The departure from Gaussian distribution can be quantified by using the fourth statistical moment *Flatness* [37], sometimes called *Kurtosis*.

$$F\left[v\right] = \left\langle \frac{\left(v - \langle v \rangle\right)^4}{\sigma^4\left[v\right]} \right\rangle, \tag{4}$$

where $\sigma\left[v\right]$ is the standard deviation of v. F is a non-dimensional quantity and it reaches the value of 3 for a Gaussian distribution and it diverges for polynomial distributions. The special value of 3 is depicted in Figure 10 by solid black line. In the case of superfluid helium, it has been proven,

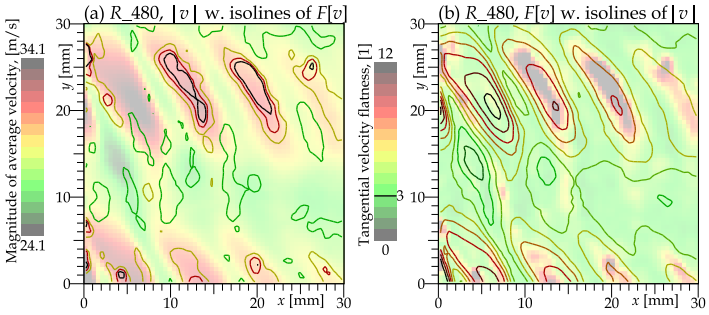

Figure 11. Direct comparison of spatial distribution of tangential velocity flatness ($F[v]$) with average velocity magnitude (w). Plane R_{480}, Mach number Ma $= 0.4$, ratio $u/c = 0.55$ and stator angle $\vartheta = 3.27°$.

that large flatness of tracer velocity is caused by the presence of highly localized quantized vortices, which change the distribution from the Gaussian to polynomial [38]. In the case of classical turbulence, values larger than 3 are generally connected with rare strong events, which relates to *intermittent effects* [37]. At higher planes, the spots of large flatness located at the cross-sections of rotor jet and stator jet (see Figure 11), where the flow is generally more quiet than in the wake, but from time-to-time, these areas are visited by some vortex or other turbulent structure, which affects the TKE not much due to its rareness, but it significantly increases the flatness there.

The correspondence with areas of cross-sections of stator and rotor jets is supported by Figure 11 showing spots of high flatness exactly in the spots of high velocity magnitude, except for the first spot from the left, which is so close to the rotor wheel that the flow is disturbed here regularly.

Close to the hub in the plane R_{445} (Figure 10(d)), we see more or less the Gauss value of flatness everywhere, because this area feels high level of turbulence all times; the strong secondary flows mix the jets and wakes completely.

We can ask not only, *where* are the structures responsible for skewness and flatness, but also, how *big* are they. Figure 12 shows the dependence of skewness and flatness on the wave number k of fluctuations. The method of extracting fluctuations of specific length-scale interval will be explained later. The skewness originates in larger structures (smaller k) for all cases, strongestly for R_{460}, at middle scales, the statistics is less skewed, but it is still positive. At small scales (large k), $S[v](k)$ increases again and the values are similar around 0.6, except for the plane closest to the hub, whose small-scale fluctuations seem to behave similarly as at middle scales. The flatness is increased by spatial variations, therefore it displays values significantly larger than 3 at all scales and all planes. Smaller scales (larger k) produce more flatness, especially in both lower planes. At larger scales (small k), the flatness of tangential velocity is largest for the plane R_{460}. Otherwise, higher planes display less flatness of this velocity component (that includes ensemble and spatial variations as well).

4.4. Size of fluctuation structures

The autocorrelation function $R_{uu}(\vec{x};\vec{y})$ [39] shows the statistical correlation of axial velocity u between two positions $\vec{x}$ and $\vec{y}$ over the ensemble of N points (i.e. frames in our movie):

$$R_{uu}(\vec{x};\vec{y}) = \frac{1}{N\sigma[u(\vec{x})]\,\sigma[u(\vec{y})]} \sum_{t=0}^{N} u(\vec{x},t)\cdot u(\vec{y},t), \tag{5}$$

where $\sigma[u(\vec{x})]$ denotes the standard deviation of u at point $\vec{x}$:

$$\sigma[u(\vec{x})] = \sqrt{\left\langle \left(u(\vec{x}) - \langle u(\vec{x})\rangle\right)^2 \right\rangle}. \tag{6}$$

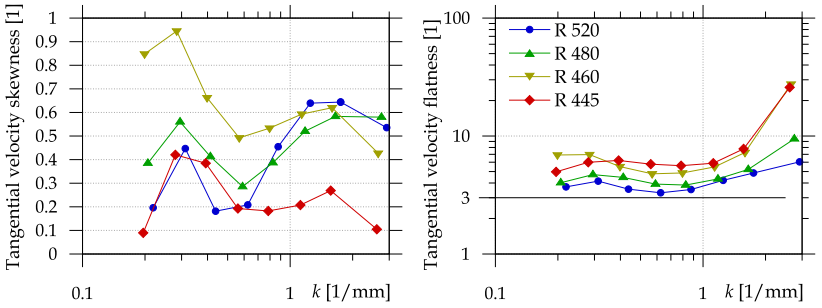

Figure 12. Skewness (left) and flatness (right) at different wave numbers k at nominal state, i.e. $u/c = 0.55$ at Ma $= 0.4$, stator angle is $\vartheta = 3.27°$, planes are different. Note that the statistical moments are calculated from the entire FoV, therefore spatial variations count as well as the temporal ones.

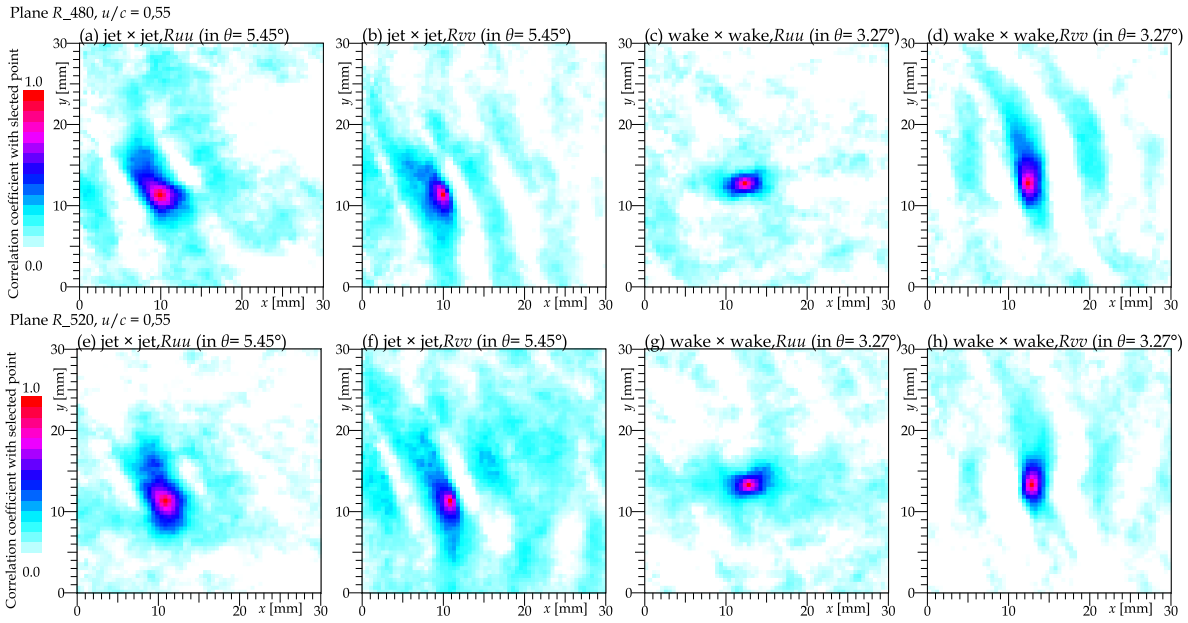

Figure 13. Spatial map of autocorrelation function of axial velocity component (panels (a, c, e, g)) and tangential velocity component (b, d, f, h) with a point at the cross-section of stator jet and rotor jet (panels (a, b, e, f)), which are taken from the data sets with stator angle $\vartheta = 3.27°$ at plane R_{480} (panels (a, b, c, d)) or R_{520} (panels (e, f, g, h)) at $u/c = 0.55$, and at the cross-section of stator wake and rotor wake (panels (c, d, g, h)), which are taken from data sets with stator angle 5.45° of the same planes and regime.

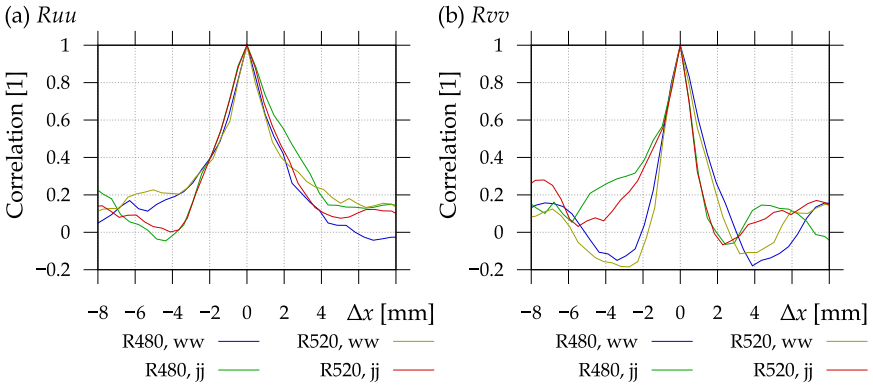

Figure 14. Autocorrelation R_{uu} (a) and R_{vv} (b) as a function of stream-wise shift from the probed point. In the legend, *ww* stands for *cross-section point of stator wake and rotor wake*, while *jj* abbreviates *cross-section point of stator jet and rotor jet*.

For the sake of convergence, the correlation function has to be ran on the *Reynolds decomposed* velocity field [40–42], which means subtracting the ensemble-average velocity. The point $\vec{y}$ we choose in fixed location at the cross-section of stator and rotor wakes (Figure 13(c)) or jets (Figure 13(a)), while the point $\vec{x}$ scans the entire field of view. Analogically to (5) the correlation R_{vv} the tangential velocity component is constructed and plotted in Figure 13(b,d).

Physically, it represents the area, where the fluctuations are correlated with the probed point and the size of this area refers to the typical size of turbulent structures. We see, that the size of fluctuations corresponds to the cross-sectional size of the rotor blade distance at both probed locations. Additionally, a weak signal from the neighboring rotor wakes (or weaker for jets) can be observed in the spatial distribution of R_{vv} (Figure 13(d)). This suggests the existence of structures larger than the inter-blade distance developed probably up-stream of the rotor wheel or even up-stream of the stator wheel.

The central peak of R_{uu} in an ideally resolved data would have a shape of a parabola, whose half-width corresponds to the Kolmogorov dissipative length-scale [43–46]. In our case (see Figure 14) the peaks are sharp suggesting, that we are missing a significant part of the energy cascade towards the small-scales. This is the limitation by the resolution of the PIV system, which is limited by the ratio of smallest to larges resolved scales by 62, which is definitely insufficient for such a complicated flow problem. On one hand, we wish to see the large patterns caused by the geometry (achieved), on the other, we want to see all vortices down to the smallest ones (not achieved). A positive statement is, that the current resolution is larger than the turbulent integral length-scale, therefore we can see at least the large turbulent vortices, which are responsible for the largest part of turbulent kinetic energy.

We venture to roughly estimate the integral length-scale based on *spatial* fluctuations. In hydrodynamic research, the integral length-scale L is usually calculated by using time-resolved stream-wise velocities at single points. Those data are usually obtained by using hot wire anemometry (HWA) technique and the time-series is transformed into distance by using Taylor's frozen turbulence hypothesis [47]. In our case, the correlation R_{uu} between pair of points is used as in equation (5):

$$L[uu]\left(\vec{x}\right) = \iint_{|\vec{x}-\vec{y}|<\Omega} \frac{R_{uu}\left(\vec{x};\vec{y}\right)}{2\pi\left|\vec{x}-\vec{y}\right|} \mathrm{d}S, \tag{7}$$

where the Ω is the radius of the neighborhood of the probed point $\vec{x}$. The term R_{uu} has to be divided by the circumference $2\pi\left|\vec{x}-\vec{y}\right|$ in order to eliminate the area grow with distance. The inconvenient property of this formula is that $L[uu]$ is not calculable everywhere in the field of view – there remains a border of undefined values, see Figure 15. Another property of this formulation is that the value at $\vec{x}$ depends on all data up to the distance Ω, thus it blurs the average flow patterns.

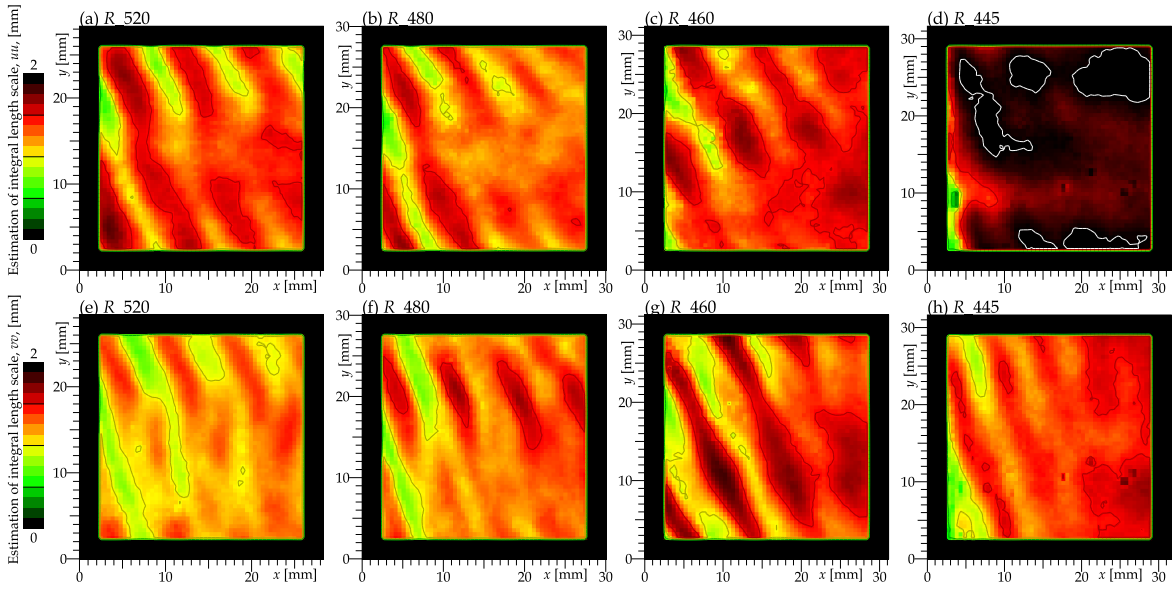

Figure 15. Spatial map of the rough estimation of the integral length scale of each velocity component (the top panels (a) – (d) represent the L of axial component, the bottom panels (e) – (h) the tangential component). Observed values fit under 2 mm except for plane R_{445}, where the spots of $L[uu] > 2$ mm are circled by white isolines. The black border around each dataset is caused by the need of certain neighborhood along each investigated point, and such a neighborhood would be not consistent when we are too close to the edge of a FoV.

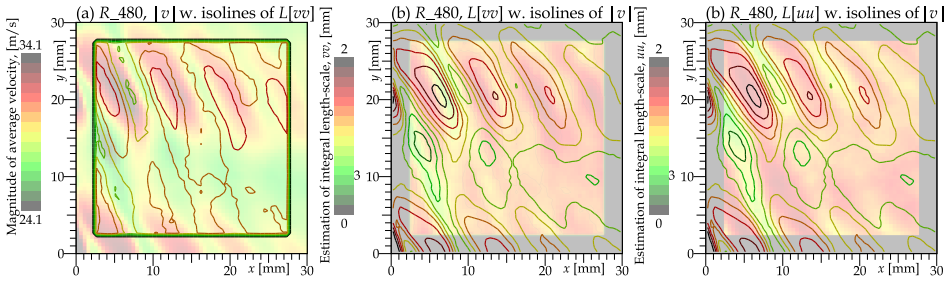

Figure 16. Direct comparison of the spatial map of the ensmeble-average velocity magnitude $|v|$ with the estimation of integral length scale $L[uu]$ and $L[vv]$ respectively.

Figure 15 shows that the variance of L is not high, it fits into an interval $0.5 - 2.0$ mm almost everywhere for the correlations of both velocity components. Note, that the positions of strips of smaller and larger values do not overlay between the velocity components, which is highlighted even in Figure 16, which directly compares the spatial distribution of the in-plane velocity magnitude with the estimation of the integral length-scale. The local maxima of $L[vv]$ correspond to the shear layer past the pressure side of the blade, while the distribution of $L[uu]$ roughly follows that of the velocity magnitude. The latter is caused simply by the fact that the faster velocity spreads the same fluctuating structure over a larger area.

The contributions of different length-scales to the turbulent kinetic energy is illustrated in Figure 17. That is a quite complicated colorful plot: the different base colors (red, green and blue) represent the turbulent kinetic energy of three different size-channels: $0.5 - 0.8$ mm for red, $1.5 - 2$ mm for green and $4 - 6$ mm for the blue channel. More details about this method as well as about the method of spatial spectrum in Figure 18 can be found in our previous publication [48].

In panel (a) of Figure 17, we see the small-scale fluctuations mostly in the rotor wakes, which are stronger *and larger* when they meet with stator wakes. As the flow develops, the middle scale

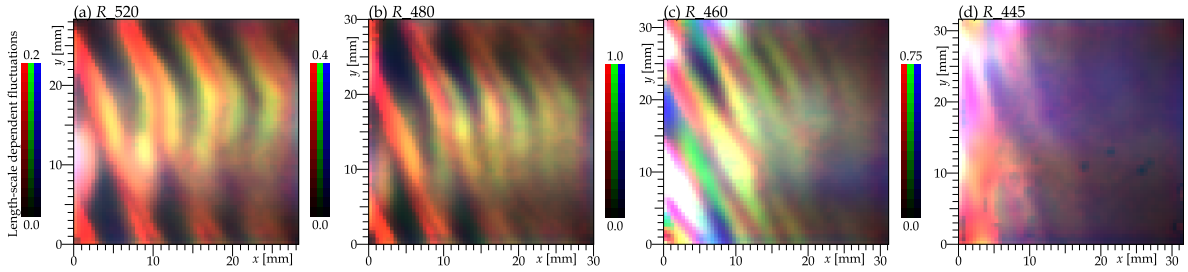

Figure 17. Turbulent kinetic energy colored via the length-scale of fluctuations causing it. The smallest scales of size $0.5 - 0.8$ mm are colored by red, green color represents fluctuations of size $1.5 - 2$ mm and the blue correspond to largest scales $4 - 6$ mm. Intensity units are arbitrary. Compare to Figure 6.

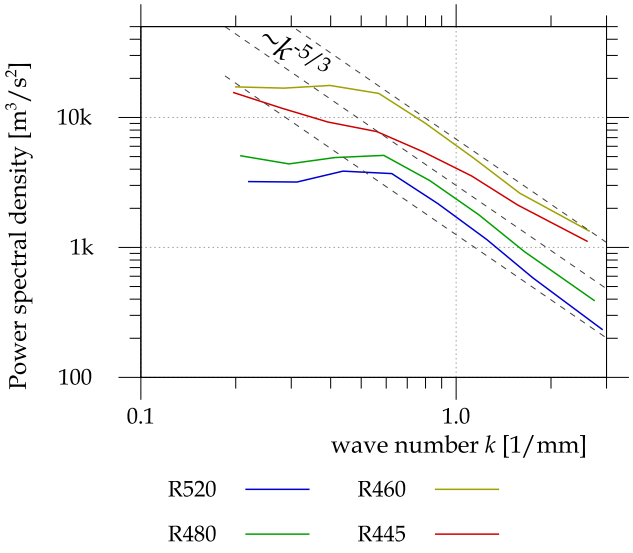

Figure 18. Spatial turbulence spectra for the investigated planes. The gray dashed lines represent the slope of the Richardson cascade [45].

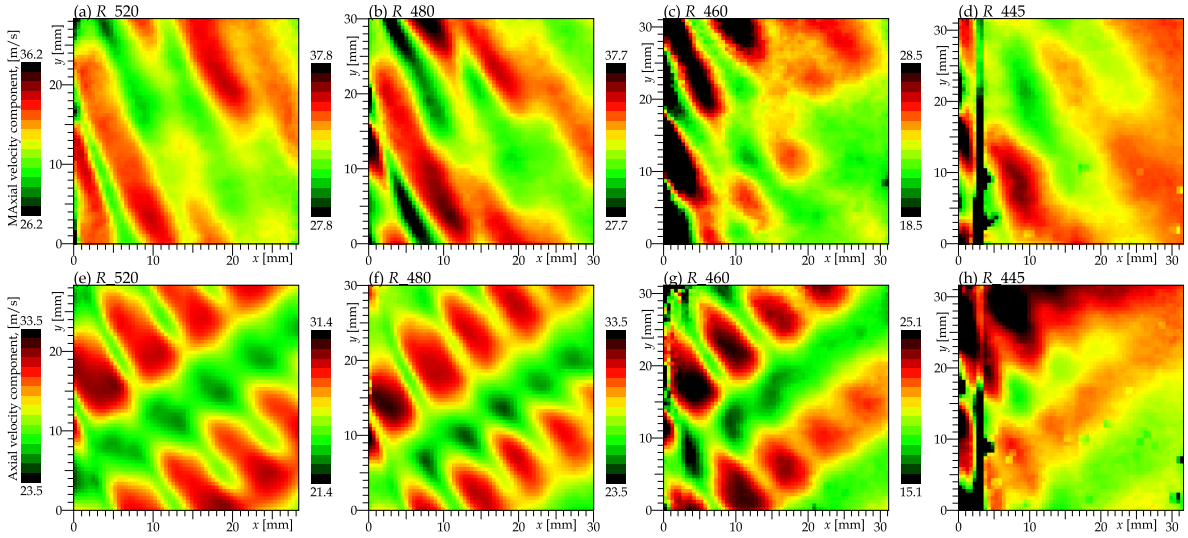

Figure 19. Ensemble averaged axial velocity component at off-design regimes $u/c = 0.4$ (top row) and $u/c = 0.7$ (bottom row). The color map shows the average axial velocity ranging $\pm 5\,\mathrm{m/s}$ around the FoV-averaged value.

(green) signal spreads over the faster weakening small scale (red) fluctuations. A similar phenomenon is observable in the plane R_{480}, panel (b) of Figure 17. But at the plane R_{460} (panel (c)), the secondary flows [49] lead to a pre-dominance of middle-scale structures and the rotor wakes are better apparent than in a pure TKE plot (Figure 6(c)). The wake displays a structure of strips of alternating *size* (not only intensity) of the turbulence. Close to the end wall (Figure 17(d)), the flow is dominated by large-scale (blue) fluctuations caused by large-scale secondary flows in that area. The rotor wake structure is only weakly observable in the small-scale (red) signal. Additionally, the picture is damaged by the already discussed optical distortion causing random (thus uncorrelated small scale) noise in the left hand side of the FoV.

The spatial energy spectrum, Figure 18, converges well to the Kolmogorov $k^{-5/3}$ spectrum at larger wave numbers (i.e. smaller length-scales of the fluctuations). The Kolmogorov theory is valid for ideal homogenous and isotropic turbulence [45] and is experimentally found in grid turbulence [30,50] and in any turbulence at length-scales smaller than the typical sizes of flow patterns, but larger than the dissipative Kolmogorov length-scale. This fact is often used in numerical simulations to reduce the number of computational cells by substituting a so-called turbulence model into length-scales smaller than a single computational cell. Our results justify this approach, because the spectra in Figure 18 suggest that the turbulence structure follows the Kolmogorov theory since the wave numbers are around $0.6\,\mathrm{mm}^{-1}$.

4.5. Off-design regimes

Two off-design regimes have been investigated, the first, overload, at relative velocity $u/c = 0.4$, the second, underload, regime at $u/c = 0.7$ (note that the nominal regime corresponds to the ratio $u/c = 0.55$). The main difference lies in the large tangential component of the stage exit velocity, which turns the stator wakes in a such way, that they cross the rotor wakes under a high angle ($u/c = 0.4$) or closer to the right angle ($u/c = 0.7$). The ensemble-averaged quantities at four explored radial planes past the rotor wheel are shown in Figures 19 – 23.

The flow conditions in regime $u/c = 0.4$ are characterized by large gradients of average tangential velocity (Figure 20) between the neighboring jets and wakes. These large gradients naturally enhance the instability and subsequent mixing of slower and faster fluid leading to larger TKE and faster decay

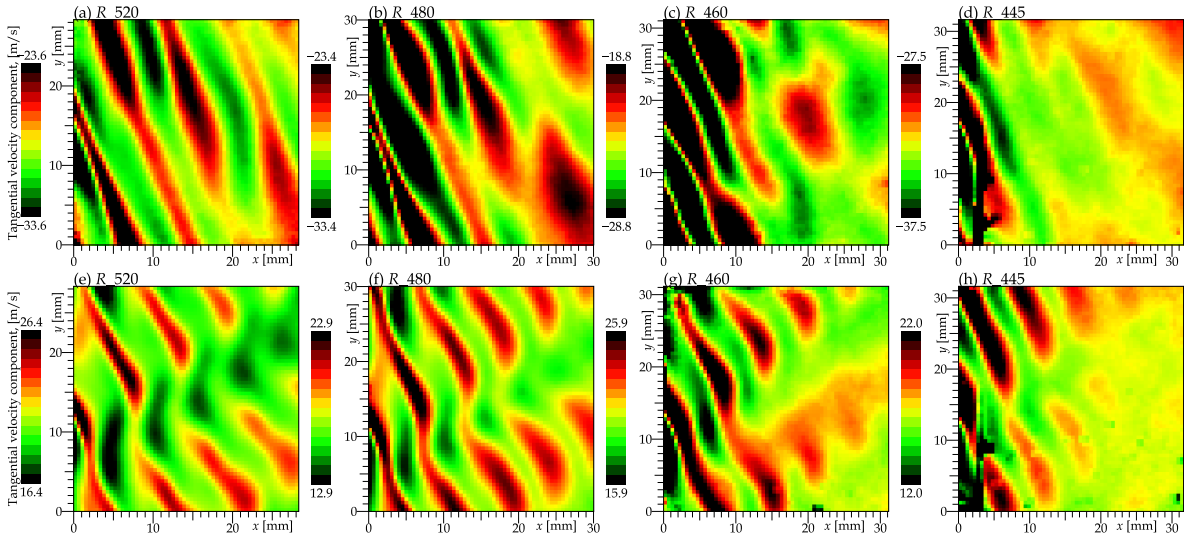

Figure 20. Ensemble averaged tangential velocity component at off-design regimes $u/c = 0.4$ (top row) and $u/c = 0.7$ (bottom row). The color map shows the average tangential velocity ranging $\pm 5\,\mathrm{m/s}$ around the FoV-averaged value.

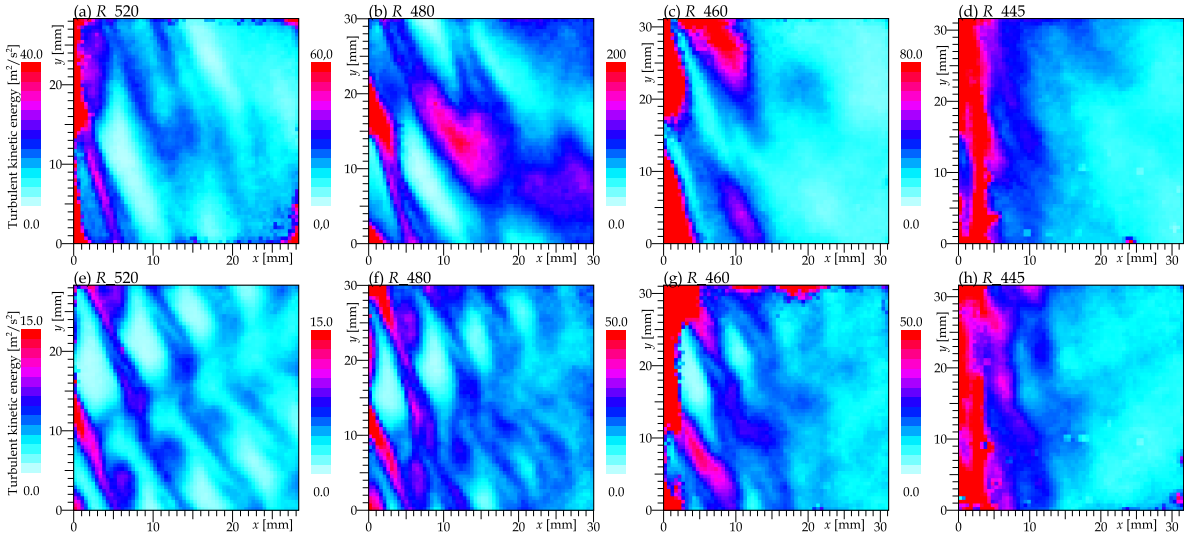

Figure 21. Turbulent kinetic energy based on axial and tangential velocity components (equation (1)) at off-design regimes $u/c = 0.4$ (top row) and $u/c = 0.7$ (bottom row). The ranges of observed values vary a lot among different planes, thus the color scale is individual for each plane.

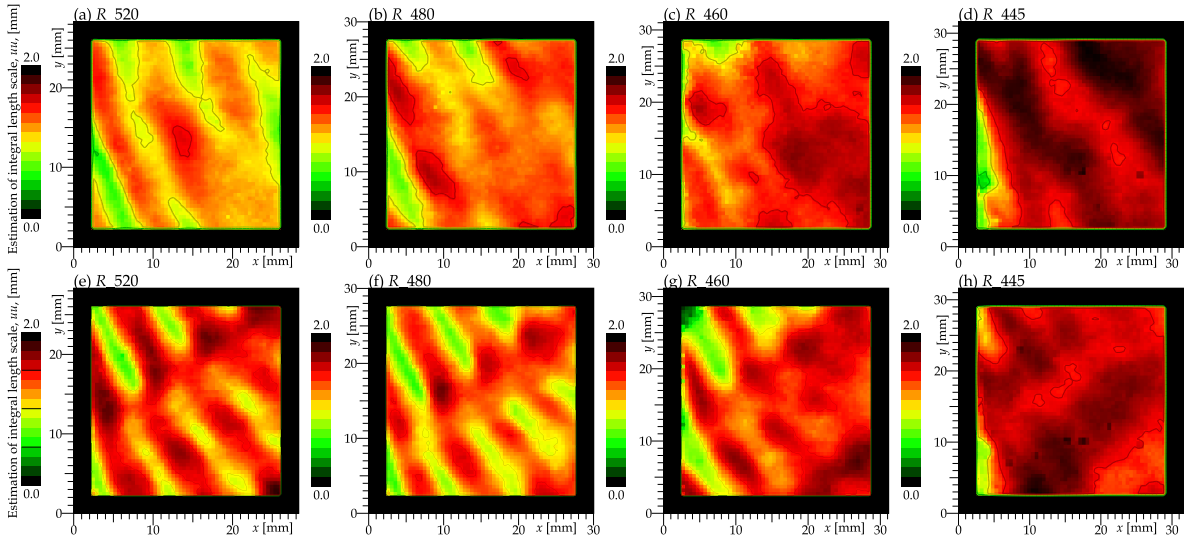

Figure 22. Rough estimation of the integral length scale calculated according to equation (7) of the axial velocity component at off-design regimes $u/c = 0.4$ (top row) and $u/c = 0.7$ (bottom row).

of these large-scale patterns. On the other hand, in regime $u/c = 0.7$, the average velocity pattern keeps almost constant strength across the entire field of view.

The figures show that there is much more turbulence in the overload regime $u/c = 0.4$ compared to nominal and underload regimes. This result is consistent with changes of reaction and rotor incidence angle. The overload regime had about a 15° higher incidence angle compared to the nominal regime. The stage reaction of 10% is much lower compared to the nominal regime. This combination leads to the increase of turbulence at the outlet of the rotor, presented in Fig. 21, due to a weaker expansion in the rotor. Higher reaction in the case of the underload regime (the reaction was 45%) caused a decrease of the turbulence at the outlet of the rotor.

In the first regime, the area of a cross-sections of stator and rotor wakes is large due to the sharp outlet angle and therefore larger (and more energetic) structures can develop inside, as it is visible in Figure 23bc as a wide spot of middle-scale fluctuations (displayed as a green color). A buffer of large-scale-energy supports the energy at smaller scales as well via the mechanism of the Richardson cascade [51,52].

The planes closer to the hub display larger estimated integral length-scale L (Figure 22) and the turbulent kinetic energy distinguished by the length-scale of fluctuations (Figure 23) shows stronger contributions of large-scale fluctuations than the mid-span and tip planes. Surprisingly, the estimated $L[uu]$ does not differ much between the overload and underload regime – everywhere we observe this quantity to lie between 1 and 2 mm with larger values towards the lower planes and increasing in downstream direction.

The spatial spectra [48] of the off-design regimes at planes R_{520}, R_{480} and R_{460} in Figure 24 show a good scaling with the Kolmogorov law except for large scales, where it differs in the shape as well as in the point of the cascade beginning. Additional difference arises at small scales, where the instrumental noise plays a role, mainly at the high velocities ($u/c = 0.4$). The universality is more supported by normalization of the spectra (Figure 24(right)). The normalization in this case has been done to the point at the middle of the observable part of the cascade.

5. Conclusion

The paper presents an experimental study of the wake of an axial single stage air turbine. The Particle Image Velocimetry (PIV) method has been used to observe the flow in axial × tangential planes, 3 × 3 cm just behind the rotor blades at different radial positions. The unique design of the

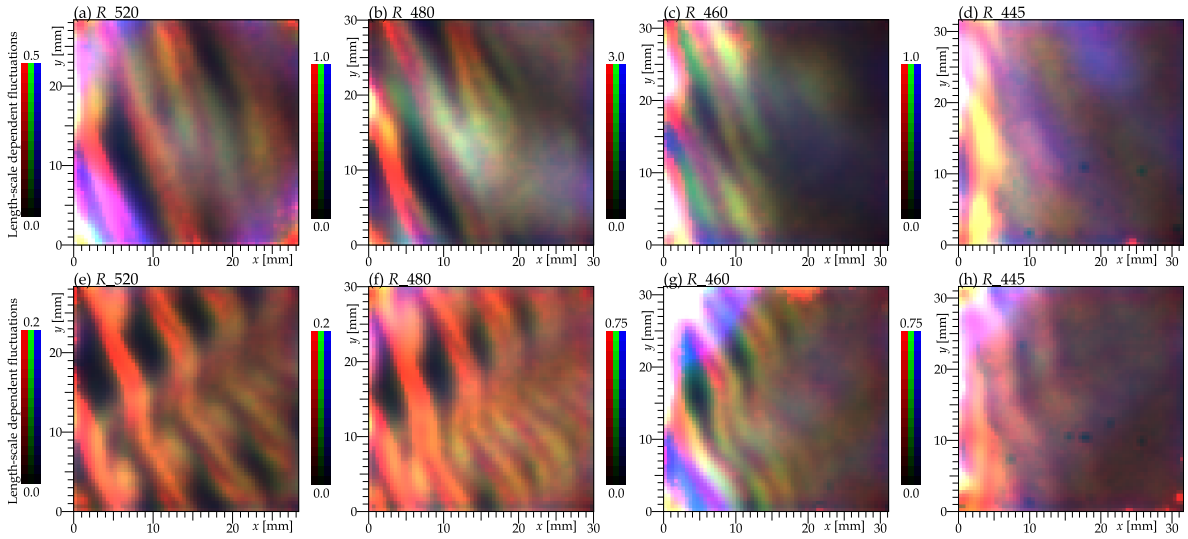

Figure 23. The turbulent kinetic energy colored by the length-scale of fluctuations. The scale is different among planes, but among different length-scale channels, the relative intensities are adapted to the Kolmogorov scaling. The red channel corresponds to fluctuations of smallest size around $0.5 - 0.8$ mm, the green color represents fluctuations of size $1.5 - 2$ mm and the blue one corresponds to scales of $4 - 6$ mm.

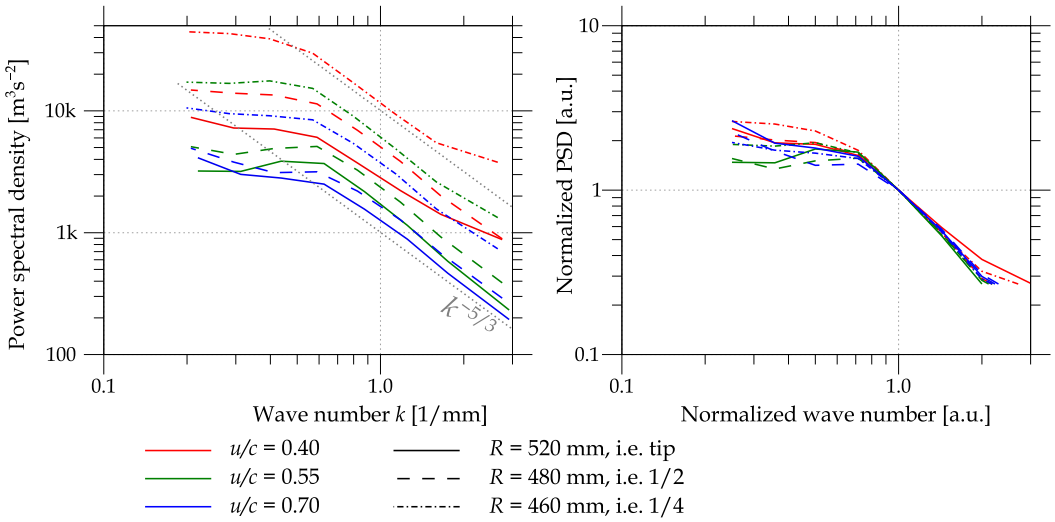

Figure 24. Spatial spectra of the three explored regimes depicted by colors and at three of four explored radii distinguished via the line style. The right panel shows the same data as the left one normalized to the middle of the Richardson cascade.

test turbine at the Czech Aerospace Research Centre (VZLÚ) allows to change the angle of the entire stator wheel in order to investigate the effect of the position of the stator wake with respect to the rotor wakes. Test were carried out under nominal conditions ($u/c = 0.55$) and two off-design regimes ($u/c = 0.4$ and $u/c = 0.7$), all at the isentropic stage Mach number 0.4.

In the investigated range of flow conditions the following observations are made:

- The wake system of the stator blades is still observable after passing the rotor wheel as put into evidence in the plots of the ensemble averaged velocity.
- The turbulent kinetic energy is largest at the cross-section of the shear layers of both wake systems.
- Large structures of the wakes as well as the upper part of the inertial range are clearly identified, but the small dissipative scales are invisible with the current setup.
- The scale of fluctuations reflects the shear layer thickness at the higher radii under nominal conditions.
- Close to the end-wall, there are flow structures of length-scale larger than the shear layers thickness. Therefore the optimization of turbine does not need only the optimization of individual blades, rather it needs also some modification of hub geometry.
- The overload ($u/c = 0.4$) regime displays larger scale of fluctuations caused by the larger area of cross-sections of stator and rotor wake systems.
- The underload regime ($u/c = 0.7$) contains less turbulent kinetic energy, probably due to the smaller area of wake cross-sections, although the wakes themselves are wider as the angle of attack is not ideal for both off-design regimes. As the TKE is smaller, the wake pattern is not mixed and survives longer, which can have negative effect to the next stage.

5.1. Future research

Future investigations will focus the two- or three-dimensionality of the flow at various radii, which can be done by exploring different planes (e.g. radial $\times$ tangential) or by upgrading to the stereo PIV system [53] using a pair of cameras observing the scene under a slightly different angles.

The contemporary development of turbines relies on numerical simulations [23,54,55], therefore it would be interesting to compare our experimental results with some of them.

6. Acknowledgment

We thank Bohumil Laštovka and Jakub Pokorný for valuable technical help. We also thank Jan Uher from Doosan Škoda Power for valuable discussions preceding this measurement campaign.

This work has originated within the framework of the project TN01000007-NCE.

The presented work was financially supported by student project SGS-2019-021 (Improving the efficiency, reliability and service life of power machines and equipment 5)

7. List of symbols and abbreviations

Symbol	Meaning
β	nominal stage angle (relative to tangential direction).
c	isentropic stage velocity.
DA	degree of anisotropy, DA $= \log_2 \frac{\sigma[v]}{\sigma[u]}$.
$F[x]$	flatness i.e. fourth statistical moment of variable x, $F[x] = (x - \langle x \rangle)^4 / \sigma^4[x]$.
FoV	field of view.
k	wavenumber, unit $\left[\mathrm{mm}^{-1}\right]$.
Ma	isentropic Mach number.
PIV	Particle Image Velocimetry.
R_{xxx}	measuring plane in axial×tangential direction; xxx denotes the *diameter*, if it was a cylinder.
R_{uu}, R_{vv}	autocorrelation function of u or v velocity components respectively.
$L[uu], L[vv]$	rough estimation of the integral length-scale of u or v, $L[uu]\,(\vec{x}) = \iint \frac{R_{uu}(\vec{x};\vec{y})}{2\pi\lvert\vec{x}-\vec{y}\rvert}\,\mathrm{d}S$
$\sigma[x]$	standard deviation of variable x, $\sigma[x] = \sqrt{\langle x^2 \rangle - \langle x \rangle^2}$.
ϑ	turn angle of the stator wheel.
TKE	turbulent kinetic energy.
u	circumferential mid-span rotor velocity.
u	axial velocity component (parallel with x-axis).
v	tangential velocity component (parallel with y-axis).
$\lvert v \rvert$	in-plane velocity magnitude, $\lvert v \rvert = \sqrt{u^2 + v^2}$.
ω	in-plane vorticity, $\omega = \Delta u / \Delta y - \Delta v / \Delta x$.

7.

1. Michelassi, V.; Wissink, J.; Rodi, W. Analysis of DNS and LES of Flow in a Low Pressure Turbine Cascade with Incoming Wakes and Comparison with Experiments. *Flow, Turbulence and Combustion* **2002**, *69*, 295–330. doi:10.1007/s10494-005-9007-1.
2. Tropea, C.; Yarin, A.; Foss, J.F. *Springer Handbook of Experimental Fluid Mechanics*; Springer, Heidelberg, DE, 2007; p. 1557.
3. Zaccaria, M.A.; Lakshminarayana, B. Unsteady flow field due to nozzle wake interaction with the rotor in an axial flow turbine: Part ii-rotor exit flow field. *Journal of Turbomachinery* **1997**, *119*, 214–224. doi:10.1115/1.2841104.
4. Chasoglou, A.; Mansour, M.; Kalfas, A.; Abhari, R. A Novel 4-sensor Fast-Response Aerodynamic Probe for Non-Isotropic Turbulence Measurement in Turbomachinery Flows. Proceedings of Shanghai 2017 Global Power and Propulsion Forum, 2017, pp. 211–1–10.
5. Ruck, G.; Stetter, H. Unsteady Velocity- and Turbulence Measurements With a Fast Response Pressure Probe. *Proceedings of the ASME Turbo Expo* **1990**, *1*. doi:10.1115/90-GT-232.
6. Antoš, P.; Uruba, V.; Jonáš, P.; Procházka, P.; Skála, V.; Hoznedl, M.; Sedlák, K. Measurement of turbulence in LP part of the 1090 MW steam turbine. XXIV Biannual Symposium on Measuring Techniques in Turbomachinery, Transonic and Supersonic Flow in Cascades and Turbomachines, 2018, MTT2418A31.
7. Barna, G. A High-Speed Photographic System for Flow Visualization in a Steam Turbine. NASA report, 1973, TM X-2763.
8. Hála, J.; Luxa, M.; Šimurda, D.; Bobčík, M.; Novák, O.; Rudas, B.; Synáč, J. Optimization of Root Section for Ultra-long Steam Turbine Rotor Blade. *Journal of Thermal Science* **2018**, *27*, 95–102. doi:10.1007/s11630-018-0989-0.
9. Porreca, L.; Hollenstein, M.; Kalfas, A.; Abharix, R. Turbulence Measurements and Analysis in a Multistage Axial Turbine. *Journal of Propulsion and Power* **2007**, *23*. doi:10.2514/1.20022.
10. Porreca, L.; Yun, Y.I.; Kalfas, A.I.; Song, S.J.; Abhari, R.S. Investigation of 3D Unsteady Flows in a Two Stage Shrouded Axial Turbine Using Stereoscopic PIV and FRAP: Part I – Interstage Flow Interactions. ASME Turbo Expo 2006: Power for Land, Sea, and Air, 2006, GT2006-90752, pp. 711–723. doi:10.1115/GT2006-90752.

11. Lang, H.; Mø rck, T.; Woisetschläger, J. Stereoscopic particle image velocimetry in a transonic turbine stage. *Experiments in Fluids* **2002**. doi:10.1007/s00348-002-0427-6.
12. Jones, R.R.; Pountney, O.J.; Cleton, B.L.; Wood, L.E.; Schreiner, B.D.J.; Figueiredo, A.J.C.; Scobie, J.A.; Cleaver, D.J.; Lock, G.D.; Sangan, C.M. An advanced single-stage turbine facility for investigating non-axisymmetric contoured endwalls in the presence of purge flow. *Proceedings of ASME Turbo Expo 2019* **2019**, *GT2019*. doi:10.1115/GT2019-90377.
13. Yun, Y.I.; Porreca, L.; Kalfas, A.I.; Song, S.J.; Abhari, R.S. Investigation of 3D unsteady flows in a two-stage shrouded axial turbine using stereoscopic PIV and FRAP - Part II: Kinematics of shroud cavity flow. Proceedings of the ASME Turbo Expo, 2006, Vol. 6 PART A, pp. 905–914. doi:10.1115/GT2006-91020.
14. Il Yun, Y.; Porreca, L.; Kalfas, A.I.; Song, S.J.; Abhari, R.S. Investigation of three-dimensional unsteady flows in a two-stage shrouded axial turbine using stereoscopic PIV - Kinematics of shroud cavity flow. *Journal of Turbomachinery* **2008**, *130*. doi:10.1115/1.2720873.
15. Göttlich, E.; Woisetschläger, J.; Hampel, B.; Jericha, H.; Heitmeir, F. Experimental investigation of unsteady effects in a transonic turbine stage. *VDI Berichte* **2004**, *1857*, 109–117.
16. Woisetschläger, J.; Pecnik, R.; Göttlich, E.; Schennach, O.; Marn, A.; Sanz, W.; Heitmeir, F. Experimental and numerical flow visualization in a transonic turbine. *Journal of Visualization* **2008**, *11*, 95–102.
17. Schennach, O.; Pecnik, R.; Paradiso, B.; Göttlich, E.; Marn, A.; Woisetschläger, J. The effect of vane clocking on the unsteady flowfield in a one and a half stage transonic turbine. *Proceedings of the ASME Turbo Expo* **2007**, *6*, 793–802.
18. Schennach, O.; Woisetschläger, J.; Marn, A.; Göttlich, E. Laser-doppler-velocimetry measurements in a one and a half stage transonic test turbine with different angular stator-stator positions. *Experiments in Fluids* **2007**, *43*, 385–393.
19. Schennach, O.; Woisetschläger, J.; Fuchs, A.; Göttlich, E.; Marn, A.; Pecnik, R. Experimental investigations of clocking in a one-and-a-half-stage transonic turbine using laser doppler velocimetry and a fast response aerodynamic pressure probe. *Journal of Turbomachinery* **2007**, *129*, 372–381.
20. Woisetschläger, J.; Lang, H.; Hampel, B.; Göttlich, E.; Heitmeir, F. Influence of blade passing on the stator wake in a transonic turbine stage investigated by particle image velocimetry and laser vibrometry. *Proceedings of the Institution of Mechanical Engineers, Part A: Journal of Power and Energy* **2003**, *217*, 385–392.
21. Woisetschläger, J.; Mayrhofer, N.; Hampel, B.; Lang, H.; Sanz, W. Laser-optical investigation of turbine wake flow. *Experiments in Fluids* **2003**, *34*, 371–378.
22. Němec, M. Turbínové stupně IR_v2-1 a IR_v2-3. Technical Report R-6948, VZLÚ, 2018.
23. Straka, P. Software pro výpočet turbulentního nestacionárního proudění s využitím nelineárního modelu turbulence. Technical Report R-6381, VZLÚ, 2016.
24. Sieverding, C.; Manna, M. A Review on Turbine Trailing Edge Flow. *International Journal of Turbomachinery, Propulsion and Power* **2020**, *5*. doi:10.3390/ijtpp5020010.
25. Hammer, F.; Sandham, N.D.; Sandberg, R.D. The Influence of Different Wake Profiles on Losses in a Low Pressure Turbine Cascade. *International Journal of Turbomachinery, Propulsion and Power* **2018**, *3*. doi:10.3390/ijtpp3020010.
26. Jašíková, D.; Kotek, M.; Horálek, R.; Horčička, J.; Kopeckỳ, V. EHD sprays as a seeding agens for PIV system measurements. *ILASS – Europe 2010, 23rd Annual Conference on Liquid Atomization and Spray Systems, Brno, Czech Republic, September 2010* **2010**, *23*.
27. Uruba, V. Decomposition methods in turbulent research. *EPJ Web of Conferences* **2012**, *25*, 01059. doi:10.1051/epjconf/20122501095.
28. Duda, D.; Jelínek, T.; Němec, M.; Uruba, V.; Yanovych, V.; Žitek, P. Particle image velocimetry measurement inside axial air test turbine - Effect of window. AIP Conference Proceedings, 2021, Vol. 2323. doi:10.1063/5.0041492.
29. Tabeling, P.; Zocchi, G.; Belin, F.; Maurer, J.; Willaime, H. Probability density functions, skewness, and flatness in large Reynolds number turbulence. *PHYSICAL REVIEW E* **1996**, *53*, 1613–1621.
30. Duda, D.; Yanovych, V.; Uruba, V. An Experimental Study of Turbulent Mixing in Channel Flow Past a Grid. *Processes* **2020**, *8*. doi:10.3390/pr8111355.
31. Choi, K.; Lumley, J.L. The return to isotropy of homogeneous turbulence. *J. Fluid Meach.* **2001**, *436*, 59–84. doi:10.1017/S002211200100386X.

32. Uruba, V. (An)isotropy analysis of turbulence. In Proceedings Topical Problems of Fluid Mechanics; Šimurda, D.; Bodnár, T., Eds., 2015, Vol. 2015, pp. 237–244.
33. Solís-Gallego, I.; Meana-Fernández, A.; Fernández Oro, J.M.F.; Argüelles Díaz, K.M.A.; Velarde-Suárez, S. Turbulence structure around an asymmetric high- lift airfoil for different incidence angles. *Journal of Applied Fluid Mechanics* **2017**, *10*, 1013–1027. doi:10.18869/acadpub.jafm.73.241.27625.
34. Romano, G. Large and small scales in a turbulent orifice round jet: Reynolds number effects and departures from isotropy. *International Journal of Heat and Fluid Flow* **2020**, *83*, 108571. doi:https://doi.org/10.1016/j.ijheatfluidflow.2020.108571.
35. Von Kármán, T. *Aerodynamics*; McGraw-Hill paperbacks : science, mathematics and engineering, McGraw-Hill, 1963.
36. Gao, J.; Guo, W.; Lvov, V.S.; Pomyalov, A.; Skrbek, L.; Varga, E.; Vinen, W.F. Decay of counterflow turbulence in superfluid 4He. *JETP Letters* **2016**, *103*, 648–652. doi:10.1134/S0021364016100064.
37. Frisch, U.; Kolmogorov, A.N. *Turbulence: the legacy of AN Kolmogorov*; Cambridge university press, 1995.
38. Mantia, M.L.; Švančara, P.; Duda, D.; Skrbek, L. Small-scale universality of particle dynamics in quantum turbulence. *Phys. Rev. B* **2016**, *94*, 184512. doi:10.1103/PhysRevB.94.184512.
39. Schulz-DuBois, E.O.; Rehberg, I. Structure Function in Lieu of Correlation Function. *Applied Physics* **1981**, *24*, 323–329.
40. Duda, D.; Uruba, V. PIV of air flow over a step and discussion of fluctuation decompositions. AIP conference proceedings, 2018, Vol. 2000, p. 020005. doi:10.1063/1.5049912.
41. Agrawal, A. Measurement of spectrum with particle image velocimetry. *Experiments in Fluids* **2005**, *39*, 836–840. doi:10.1007/s00348-005-0018-4.
42. Agrawal, A.; Prasad, A. Properties of vortices in the self-similar turbulent jet. *Experiments in Fluids* **2002**, *33*, 565–577. doi:10.1007/s00348-002-0507-7.
43. Pope, S.B. *Turbulent flows*; Cambridge University Press, Cambridge, UK, 2000; p. 771.
44. Aubry, N.; Guynnet, R.; Lima, R. Spatiotemporal analysis of complex signals: theory and applications. *Journal of Statistical Physics* **1991**, *64*, 683–739. doi:10.1007/BF01048312.
45. Kolmogorov, A.N. Dissipation of Energy in the Locally Isotropic Turbulence. *Proceedings of the Royal Society A: Mathematical, Physical and Engineering Sciences* **1991**, *434*, 15–17. doi:10.1098/rspa.1991.0076.
46. Barenghi, C.F.; Sergeev, Y.A.; Baggaley, A.W. Regimes of turbulence without an energy cascade. *Scientific Reports* **2016**, *6*, 1–11, [1609.09705]. doi:10.1038/srep35701.
47. Cheng, Y.; Sayde, C.; Li, Q.; Basara, J.; Selker, J.; Tanner, E.; Gentine, P. Failure of Taylor's hypothesis in the atmospheric surface layer and its correction for eddy-covariance measurements. *Geophysical Research Letters* **2017**, *44*, 4287–4295. doi:doi.org/10.1002/2017GL073499.
48. Duda, D.; Uruba, V. Spatial Spectrum From Particle Image Velocimetry Data. *ASME J of Nuclear Rad Sci.* **2019**, *5*. doi:10.1115/1.4043319.
49. Ilieva, G.I. A deep insight to secondary flows. *Defect and Diffusion Forum* **2017**, *379*, 83–107. doi:10.4028/www.scientific.net/DDF.379.83.
50. Kurian, T.; Fransson, J.H.M. Grid-generated turbulence revisited. *Fluid Dynamics Research* **2009**, *41*, 021403. doi:10.1088/0169-5983/41/2/021403.
51. Richardson, L.F. *Weather prediction by numerical process*; Cambridge University Press, 1922.
52. Yang, X.; Lozano-Durán, A. A multifractal model for the momentum transfer process in wall-bounded flows. *Journal of Fluid Mechanics* **2017**, *824*. doi:10.1017/jfm.2017.406.
53. Regunath, G.S.; Zimmerman, W.B.; Tesař, V.; Hewakandamby, B.N. Experimental investigation of helicity in turbulent swirling jet using dual-plane dye laser PIV technique. *Experiments in Fluids* **2008**, *45*, 973–986. doi:10.1007/s00348-008-0515-3.
54. Sanders, D. CFD modeling of separation and transitional flow in low pressure turbine blades at low Reynolds number. PhD thesis, Virginia Polytechnic Institute, 2009.
55. McQuilling, M. Design and validation of a high-lift low-pressure turbine blade. PhD thesis, Wright State University, 2007.